


Unconventional electromagnetic properties of the graphene quantum dots

S. E. Shafraniuk 

Tegri LLC, 558 Michigan Ave, Evanston, Illinois 60202, USA



(Received 10 January 2019; published 2 August 2019)

Quantum dots based on the graphene stripes show unconventional optical properties in the THz frequency range. The graphene quantum dot (GQD) is made of an electrically gated stripe with zigzag edges. Inside the active region (AR), which is enclosed between the source and drain electrodes, there are two sharp energy (\pm) levels, whose separation 2Δ is controlled with Stark effect by applying the lateral dc electric field. Such edge states determine the unique nature of elementary excitations, chiral fermions, that are responsible for the nonlinear optical response revealing a potential for many applications. They are, e.g., the frequency multiplication and self-focusing of two-dimensional solitons. Furthermore, when injection of the nonequilibrium electrons causes an inverse population of the levels localized in AR, the subsequent recombination of electrons and holes leads to a coherent emission of the THz waves.

DOI: [10.1103/PhysRevB.100.075404](https://doi.org/10.1103/PhysRevB.100.075404)

Unconventional optical properties of graphene in the THz range with frequencies $f = 0.5\text{--}100$ THz attract significant attention of many researchers [1–7]. Interest in the THz waves (T rays) is motivated by a variety of potential applications in medicine, information technology, communication, and security. One example of the T-ray application is the remote sensing of chemical and biological substances that requires powerful THz lasers and high-resolution spectral analyzers. There are also suggestions of quantum dot THz detectors [5,6], frequency multipliers [8–10], and self-focusing of two-dimensional solitons [11] in the electrically tunable metastructures. Recently reported [5,6] carbon nanotube THz receivers and spectral analyzers exploit the field-induced single-electron tunneling and transitions between the quantized electron levels. Furthermore, unique plasmonic characteristics of graphene allow building the tunable THz lasers [7]. The surface plasmons (SP), whose spectrum changes versus the applied gate voltage, have been observed in several experiments [12–22] on graphene.

One remarkable feature of graphene is that the carrier concentration, the electrochemical potential μ , and hence its conductivity σ can be appropriately tuned, e.g., by applying appropriate electric potentials to the gate electrodes [12, 23–25]. Hence, optical properties of the 2D atomic monolayers are readily tunable in the terahertz (THz) spectral region [12,26], enabling their application in the compact electrically controllable THz optical devices [27]. These open new opportunities as compared to the noble metals that are typically used in THz devices [23]. Hence, the SP spectrum in the 2D atomic monolayers is altered *in situ*, without any changes in the device’s design while optical and plasmonic characteristics of the 2D materials are tunable in the terahertz (THz) spectral region [12,26].

Currently, there are several concepts of the THz emitters made of the carbon nanotube and graphene [12–15]. A lot of attention is paid to the solid state laser involving localized quantum states arising in systems with reduced dimensionality, e.g., 2D (quantum wells) or 1D (quantum dots). One

example is the quantum cascade lasers (QCL) based on layered semiconducting superlattices where a series of quantum wells with 2D electron spectrum is created. A “proof of concept” tunable THz laser based on the gain modulation by graphene plasmons in an aperiodic lattice and exploiting the unique properties of graphene plasmons was built and tested in Ref. [7]. However, despite their remarkable performance, such quantum cascade lasers (QCL) have serious setbacks. A basic problem is that the energy dissipation caused by electron-phonon and electron-electron collisions leads to considerable intrinsic Joule heating raising the internal local temperature far above the temperature of the external environment. Such local Joule heating causes an adverse negative effect on the QCL performance. To reduce the negative effect of the local heating, one should decrease the bias current below some threshold value and also cool down the QCL structure below 200 K. The above measures complicate the QCL design and limit the QCL system power and efficiency. Also there are several concepts of the THz emitters made of the carbon nanotube and graphene [12,13]. A “proof of concept” tunable THz laser based on the gain modulation by graphene plasmons in an aperiodic lattice and exploiting the unique properties of graphene plasmons was built and tested in Ref. [7].

A possible fundamental solution to the above issue of overheating represent systems with lowered dimensionality, e.g., with 1D or even 0D instead of 2D. The electron bands in the 1D and 0D systems are much narrower than in the 2D systems, which also means that the phase space where the electron-phonon scattering occurs is reduced and most of the electron-phonon scattering processes are eliminated. Hence, in the 1D and 0D systems, the intrinsic energy dissipation due to suppression of the electron phonon scattering is considerably lowered as well. This motivates the interest to electromagnetic properties of low-dimensional comprising quantum dots. Promising examples are the novel 2D atomic monolayers like graphene and its allotropes. The graphene stripes and carbon nanotubes represent 1D systems, whose

dimensionality is reduced further to 0D by introducing an additional confinement by placing electrodes and local gates. Basically, quantum dot QD lasers are good candidates for the next generation high-speed communication and already are more promising than quantum well lasers with respect to important features like threshold current, temperature stability, chirp, and feedback insensitivity [28–31]. However, there is a need to understand what limits the performance and how it can be improved. This requires a better understanding of the underlying dynamics on a microscopic level. Below we study a graphene quantum dot using microscopic approach for calculating the optical susceptibility.

In this work we consider an all-electrically controlled 0D quantum dot based on the graphene stripe with zigzag edges [42] that comprises a plasmonic THz microcavity. The motivation for this work is the recent success in synthesis of graphene stripes with perfect zigzag edges [32] where according to Refs. [33–36] the topologically protected, sharp, and voltage-controlled edge energy levels emerge. Below we will see that exploiting such stable, voltage-controlled edge energy levels opens new opportunities for designing the tunable THz devices. We utilize the unique intrinsic properties of graphene that allow for building various devices with novel remarkable properties. The study is focused on the ability of graphene quantum dot (GQD) to dynamically modulate round-trip modal gain values and shows potential for forming the laser emission. Such gated 2D monolayer material serves as a powerful tool to control the optical properties of GQD. The GQD device is instantly tunable and is all electrical in nature, with minimal electrical power demands.

The goal of this work is to compute the optical susceptibility of the graphene quantum dots (GQD) that describe their unconventional electromagnetic (EM) properties. The efforts are focused on the all-electrically controlled GQD fabricated using the graphene stripes with atomic zigzag edges. The knowledge of how the optical susceptibility of GQD depends on the frequency and electrochemical potential allows better understanding of the physical mechanisms related to the electrically controlled absorption and emission of the electromagnetic field. Furthermore, the computation results allow finding, e.g., the conditions to the THz waves emission by the all-electrically controlled GQD. Furthermore our study also focuses on finding the nonlinear electromagnetic response of GQD. We will see that the physical mechanism of such nonlinearity originates from the unconventional properties of chiral fermions in graphene stripes with atomic zigzag edges.

I. THE MODEL

Geometry of the proposed device is shown in Fig. 1(a) where the central part is the graphene stripe, whose properties are controlled by the source drain and gate electrodes. The active region represents the graphene quantum dot containing two sharp (\pm) levels originating from the edge states and spaced by 2Δ . Since the edge states are topologically protected [35], the (\pm) levels are very sharp and robust, even if the edge roughness and impurities are present. The magnitude of the level spacing 2Δ is controlled using the Stark effect by setting the electric voltage between the split gates [36]. Besides, the energy level positions E_n in the left (L) and

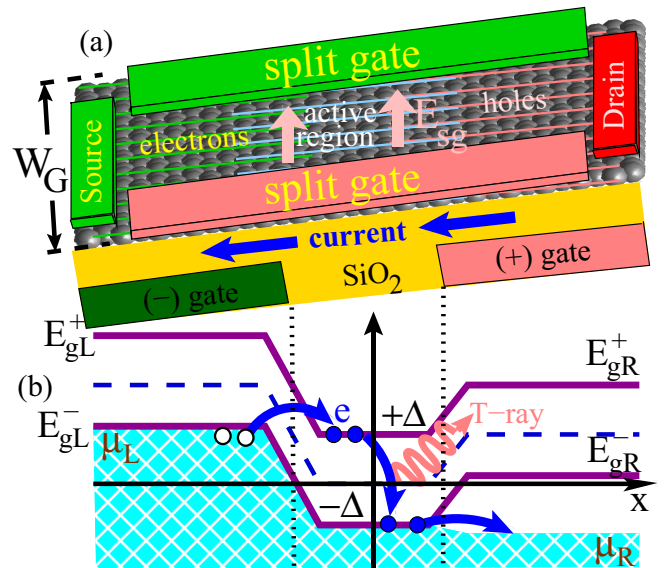


FIG. 1. (a) Geometry of the all-electrically controlled quantum dot (GQD) made of the graphene stripe with zigzag edges. The split gates form a transversal electric field E_{sg} , which due to Stark effect splits the energy 0 level into the upper (with energy $+\Delta$) and lower [with energy $-\Delta$, see sharp peaks in the electron density of states in Fig. 2(d) that originate from the (\pm) levels], whose inverse population is created when a finite bias $V_{SD} \geq 2\Delta$ is applied between the source and drain electrodes provided that the electron electrochemical potentials $\mu_{L,R}$ in the left and right banks of the graphene stripe are set, respectively, as $\mu_L = E_{gL}^-$ and $\mu_R \leq E_{gR}^- - \Delta$ using the back (\pm) gates. (b) Energy diagram of GQD.

right (R) side sections of the graphene stripe are controlled by applying electric potentials $V_{GL,R}$ to the left and right side bottom gate electrodes, respectively. Furthermore, by applying a finite bias voltage between the source and drain electrodes one injects the nonequilibrium electrons into the upper level with energy $E_+ = +\Delta$, thereby creating an inverse population of the upper (+) level in the active region. The electrons residing on the upper (+) level then recombine to the lower (-) level by emitting THz photons. Hence, the subsequent recombination of the electrons into the lower level with $E_- = -\Delta$ leads to an emission of the T rays with frequency $f = 2\Delta/h$. The interaction between light and material is controlled by the shape of the electromagnetic density of states (DOS) in the microresonator [37,38]. These mean that the magnitudes of lasing frequency f and the amplification of resonant modes are set by applying the split-gate voltage V_{SG} across the active region of the laser and/or by the source drain and bottom gate voltages as shown in Fig. 1. The latter mechanism is studied in detail below in Sec. V. We will see that the resonant frequency of THz emission depends not only on the split gate voltage V_{SG} as mentioned above but also it varies versus the electrochemical potential μ , which is controlled by applying voltage to the gate electrodes. This enables flexible all-electric manipulations of the lasing emission parameters [39–41]. Understanding the mechanisms determining the optical properties of GQD is accomplished using solutions to the Dirac equation complemented by appropriate boundary conditions (see Refs. [4,33–36,42] for details).

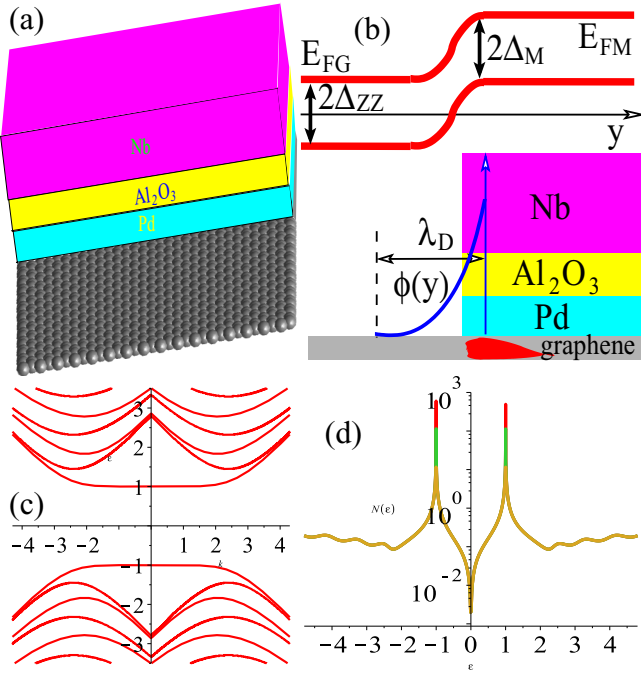


FIG. 2. (a) One side of the Nb/Al₂O₃/Pd/G gate which is deposited on the graphene stripe to form the GQD active region shown in Fig. 1. (b) The energy diagram at the graphene/gate boundary. (c) Electron spectrum showing the subband structure of GQD made of the graphene stripe enclosed between two timberlike split gate electrodes to form the active region with effective zigzag edges shown in Fig. 1(a). (d) The local electron density of states $D(\epsilon)$ inside the GQD active region. The transversal dc electric field \mathbf{E}_{sg} due to the Stark effect splits the zero-energy peak into two separate peaks forming an energy gap 2Δ .

II. SUSCEPTIBILITY OF GRAPHENE

Initially we consider the simplest case of the two-dimensional (2D) electron gas in the atomic monolayer representing a suspended pristine graphene. A general expression for the optical susceptibility of free carriers in graphene that are chiral fermions (HF) takes the form

$$\chi(\mathbf{q}, \omega) = \frac{|d_{cv}|^2}{L^2} \sum_{s,s'=\pm 1} \int \frac{d^2\mathbf{k}}{(2\pi)^2} \frac{f(\epsilon_{s,\mathbf{k}+\mathbf{q}}) - f(\epsilon_{s',\mathbf{k}})}{\omega - \epsilon_{s,\mathbf{k}+\mathbf{q}} + \epsilon_{s',\mathbf{k}} + i\eta} \quad (1)$$

where d_{cv} is the electric dipole matrix element, whose indices c, v are attributed to the conducting/valence bands, L is the size of a square-shaped 2D sample, η is the damping parameter associated with the electron energy dissipation during the inelastic collisions, \mathbf{k} is the 2D electron momentum, \mathbf{q} and ω are the respective electron momentum and energy change, $f(\epsilon_{s,\mathbf{k}})$ is the HF distribution function that depends on the HF excitation energy $\epsilon_{s,\mathbf{q}}$, which for the pristine graphene conforms to the continuous dispersion law

$$\epsilon_{s,\mathbf{q}} = sv_F|\mathbf{q}| \quad (2)$$

where s and $s' = \pm 1$ are the HF branch indices, and v_F is the Fermi velocity in graphene. The damping parameter η in Eq. (1) actually plays the same role as a parameter of the

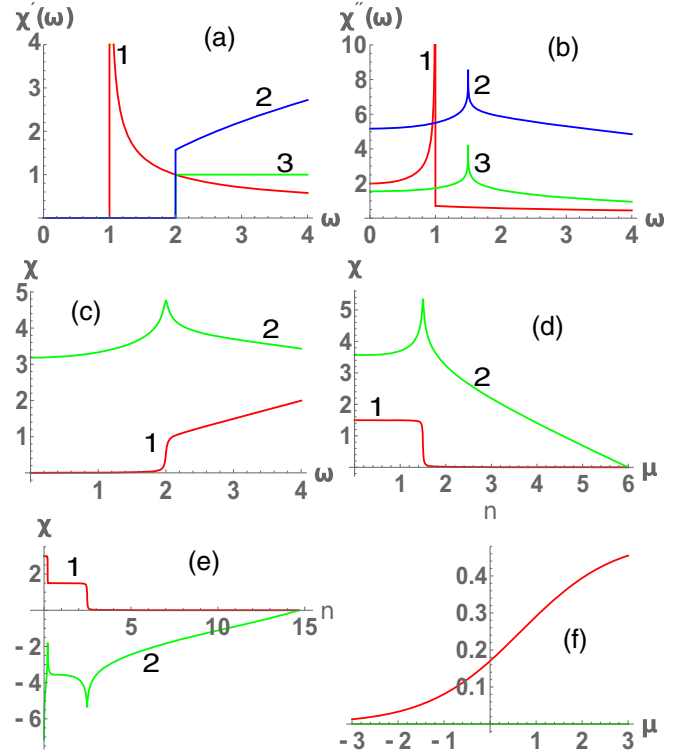


FIG. 3. Optical susceptibility: (a) $\Re\chi(\omega)$ for $D = 1 \dots 3$ (respective curve labels are 1, 2, and 3), $\delta = 1$, $\mu = 0.5$, and $\Lambda = 36$. (b) $\Im\chi(\omega)$ for $D = 1 \dots 3$ (respective curve labels are 1, 2, and 3), $\delta = 1$, $\mu = 0.5$, and $\Lambda = 16$. (c) and (d) The real (curve 1) and imaginary (curve 2) parts of the pristine graphene susceptibility $\chi(\omega)$ [see (c) for $\mu = 1$] and $\chi(\mu)$ [see (d) for $\omega = 3$], respectively, versus the frequency ω and electrochemical potential μ for $\eta = 0.02$, $\Lambda = 6$. (e) The real (curve 1) and imaginary (curve 2) $\chi(n)$ for the pristine graphene for $\eta = 0.2$, $\Lambda = 6$, $\mu = 1$. (f) The HF excitations concentration $n(\mu)$ versus the electrochemical potential μ for pristine graphene.

adiabatic switch-on. For the HF spectrum (2), the density of states is [42]

$$D_G(\epsilon) = \frac{3\sqrt{3}a^2}{\pi v_F^2} |\epsilon|, \quad (3)$$

where a is the lattice constant in graphene.

The calculation details of the optical susceptibility are given in Appendix. Results of the calculation are illustrated in Fig. 3 where we show the real $\chi' = \Re\chi$ and imaginary $\chi'' = \Im\chi$ parts of the optical susceptibility versus the frequency ω and electrochemical potential μ . As an illustration, we also show results for a conventional semiconductor with dimensionalities $D = 1, 2, 3$ [see Figs. 3(a) and 3(b)]. Parameters of the calculations, whose details are given in Appendix, are indicated in the caption. Respective results for $\Re\chi(\omega)$ (curve 1) and $\Im\chi(\omega)$ (curve 2) of the pristine graphene are shown in Fig. 3(c) while Fig. 3(d) illustrates results for $\Re\chi(\mu)$ (curve 1) and $\Im\chi(\mu)$ (curve 2). Figure 3(e) shows the results for χ versus the charge carrier concentration n , as indicated in the caption. The last Fig. 3(f) shows dependence of the HF charge carrier concentration n versus the electrochemical potential μ for pristine graphene.

At finite temperatures and in the nonequilibrium conditions, the respective calculations of $\chi(\omega, \mu)$ are conducted numerically. Numeric solutions are also useful when considering graphene-based structures with more complicated excitation spectrum. Below we study the optical properties of the graphene stripe with zigzag edges and nonlinear optical properties of GQD when a strong ac field is present.

III. ZZ STRIPE OF GRAPHENE

For graphene stripes, whose width W is finite, one should also consider quantization of the HF excitations in the lateral direction. Below we compute optical susceptibility of the graphene stripe with atomic zigzag edges. We use units with $\hbar = 1$ and $k_B = 1$ if not stated otherwise. The edge states [4,33–36,42] emerging in the graphene stripe change the HF excitation spectrum significantly. This happens because the chirality of excitations in graphene imposes additional constraints on reflection processes due to conservation of two pseudospins. A transverse d.c. electric field $\mathbf{E} = \{0, E_y, 0\}$ is applied perpendicular to the graphene stripe axis utilizing the split gate electrodes shown in Fig. 1(a). When $E_y = 0$, the electron reflections at the atomic zigzag edges [33,34,36] cause a crisp narrow energy level to arise at the energy $\epsilon = 0$. When the transverse electric field is finite, $E_y \neq 0$, such the zero-energy level experiences Stark splitting, whose magnitude is $2\Delta = 2eE_yW$ (see Refs. [4,35,36,42]). Then, the Stark splitting of the sharp singularities at energies $\epsilon = \pm\Delta$ emerging in the electron density of states [see Fig. 2(d)] is controlled by the electric field $E_y \neq 0$. Below we will see that such the electrically controlled HF spectral singularities are responsible for the remarkable optical properties of the graphene quantum dots. The effect is described in terms of the susceptibility $\chi(\omega, \mu)$, which we compute below. An additional control of $\chi(\omega, \mu)$ is introduced with the top (or bottom) local gate electrodes [see Fig. 1(a)]. Thus, the respective local gate voltages control the both, the Stark splitting Δ along with the HF electrochemical potential μ . Below we will see that the shape of $\chi(\omega, \mu)$ depends on both μ and Δ .

There is no simple analytical expression for the HF excitation energy in the graphene stripe with atomic zigzag edges [4,33–36,42]. The HF dispersion law [4,33–36,42] is given by the two equations

$$\epsilon_k = \mu \pm \sqrt{\Delta^2 + k_y^2 v_F^2 + k_x^2 v_F^2} \quad (4)$$

$$k_y = \frac{k_x}{\tan(Wk_x)} \quad (5)$$

that describe the constrain due to the pseudospin conservation during elastic reflections of the HF excitations on atomic edges. The electron energy in graphene stripe (4) depends on the two components of the electron (HF) momentum, k_y (longitudinal) and k_x (transversal), which are related by Eq. (5). In an infinitely long stripe by width W , k_y is continuous while k_x discrete, because the transversal momentum is quantized. In the geometry in Fig. 1(a), the active region length L_a is $L_a \gg W$, therefore the quantization along the y axis is negligible. We will see that such the constrain allows reducing the dimensionality of the system from 2D as in pristine graphene to 1D for the stripe. In Eqs. (4) and (5), ϵ_k is the HF energy

variable, μ is the electrochemical potential, $\Delta = eE_yW$ is the Stark splitting of the zero-energy level posing as the “energy gap” in Eq. (4). In such a case, the splitting energy also depends on the gate efficiency α . Magnitude of μ is controlled by the bottom (or top) gate electrodes, while Δ is controlled by the split gate electrodes depicted in Fig. 1(a) as illustrated by the energy diagram in Fig. 1(b). The HF dispersion law is computed by solving Eqs. (4) and (5). The HF excitation energy $\epsilon(k_y)$ in the graphene stripe with zigzag edges is shown in Fig. 2(c) versus the longitudinal momentum k_y . Technically, the electron density of states shown in Fig. 2(d) is computed as

$$D_{ZZ}(\epsilon) = \left| \frac{dk_y(k_x)}{d\epsilon_k} \right| = \left| \frac{dk_y(k_x)}{dk_x} \right| / \left| \frac{d\epsilon_k}{dk_x} \right|, \quad (6)$$

which gives an analytical expression

$$D_{ZZ}(\epsilon) = \left| \frac{\epsilon_k \tan k_x W - k_x W (\tan^2 k_x W + 1)}{k_x \tan^2(k_x W)} \right|, \quad (7)$$

where according to Eqs. (4) and (5), k_x depends on the energy variable ϵ . To compute $\chi(\omega, \mu)$ for the quasi-1D graphene stripe with atomic zigzag edges, we again use the general expression Eq. (1). The calculation is simplified for the direct interband transitions ($\mathbf{q} = 0$). Then we get

$$\begin{aligned} \chi(\omega) &= \frac{|d_{cv}|^2}{2\pi a^2} \int \frac{[f(\epsilon_k - \mu) + f(\epsilon_k + \mu) - 1]}{\omega \pm 2\epsilon_k + i\eta} dk_y dk_x \\ &= \frac{|d_{cv}|^2}{2\pi a^2} \int_{k_{\min}}^{k_{\max}} D_{ZZ}(k_x) [1 - f(\epsilon_k - \mu) - f(\epsilon_k + \mu)] \\ &\quad \times \left(\frac{1}{\omega - 2\epsilon_k + i\eta} - \frac{1}{\omega + 2\epsilon_k + i\eta} \right) dk_x, \end{aligned} \quad (8)$$

where we use

$$\begin{aligned} f(\epsilon_{s,k}) - f(\epsilon_{s',k}) &= f(-\mu + \epsilon_k) - f(-\mu - \epsilon_k) \\ &= \pm [f(\epsilon_k - \mu) + f(\epsilon_k + \mu) - 1] \end{aligned} \quad (9)$$

and

$$dk_y = D_{ZZ}(k_x) dk_x. \quad (10)$$

When integrating (8) in infinite limits, the respective integral diverges. Therefore we introduce cutoff by setting the lower k_{\min} and upper k_{\max} limits of integration in Eq. (8), which, respectively, are found as solutions of the equations

$$k_{\min}^2 = \mu^2 / v_F^2 - [k_y(k_{\min})]^2 - (\Delta / v_F)^2 \quad (11)$$

and

$$k_{\max}^2 = \Lambda^2 / v_F^2 - [k_y(k_{\max})]^2 - (\Delta / v_F)^2. \quad (12)$$

Above we have used that the respective change of the HF excitation energy is $-\epsilon_{s,k} + \epsilon_{s',k} = \pm 2\epsilon_k$, where ϵ_k is defined by Eq. (4). The above Eqs. (5), (11), and (12) serve as the closed system of transcendental equations allowing to finding k_{\min} and k_{\max} . From Eq. (6) one can see that in contrast to pristine graphene, whose HF density of states (3) is a smooth function of the energy variable E , the respective density of states $D_{ZZ}(\epsilon)$ given by Eq. (6) for the graphene stripe with zigzag (ZZ) edges shows dramatically different behavior, as illustrated in Fig. 2(d). Namely, owing to the

appearance of ZZ edge states in the graphene stripe, the respective singularities in the density of states (6) arise when $\tan^2(k_x W) = 0$ in the denominator of Eq. (7) provided

$$k_x = \frac{\pi}{W} m \quad (13)$$

where m is integer. One can notice the mentioned sharp singularities at energies $\epsilon = \pm\Delta$ (in units of Stark splitting Δ) in the plot of DOS in Fig. 2(d), while the singularities are smoothed at energies, $\epsilon > \Delta$ and $\epsilon < -\Delta$. The number of excitations in the ZZ graphene stripe is computed as

$$N = 2 \sum_{\mathbf{k}} f_k \rightarrow \frac{12\sqrt{3}a^2}{\pi v_F^2} \int_{k_{\min}}^{k_{\max}} D_{ZZ}(k_x) f(\epsilon_k - \mu) dk_x, \quad (14)$$

where the lower and upper integration limits are again determined by solution of Eqs. (5), (11), and (12).

The relevant energy scale in the above formulas (8)–(14) is determined by the atomic edge geometry and by the graphene stripe width W . Other energy scales in Eqs. (8)–(14) are related to ω , Δ , μ , and η . Typical magnitudes of interest here are $\omega \sim 2\pi f$, where for the electromagnetic field frequency $f = 1$ THz, the respective photon energy is $hf = 4$ meV. Then, $\mu \sim 2\Delta \sim hf = 4$ meV, and we also use $\eta \sim 0.1\Delta$. Essentially, the last parameter η , which also determines the width of quantized levels localized in the active region depends on coupling of GQD to the substrate and also by the inelastic collisions, which also depend on the temperature and GQD geometry.

IV. ELECTROMAGNETIC EMISSION FROM GQD

A fundamental problem when designing the laser for the frequency region 0.5–100 THz is that the THz photon energy E_v^T is relatively low, $E_v^T \approx 4$ – 0.4 eV, as compared to a visible light photon for which $E_v^L \approx 1.8$ – 3 eV. Therefore, to ensure a monochromatic THz emission, the width η of quantized levels localized in the active region is required to be much narrower than Δ . This problem is solved by a proper designing the active region, which is the key element of any solid state laser. Parameters of the active region must satisfy to a number of requirements, which have to be observed in order to get the T-ray emission out of it. In conventional visible light lasers, η is typically much smaller than the level spacing between the e/h levels, i.e., $\eta \ll \Delta$. Then, the photon energy E_v^L is precisely equal to the level spacing energy Δ , i.e., $E_v^L \equiv \Delta$ while the emitted light beam is fairly monochromatic and coherent. The situation is different in the THz lasers where at the bottom part of the THz domain the condition $\eta \ll \Delta$ might fail if the level broadening η exceeds Δ , which is relatively small, $\Delta \approx 4$ meV. In the latter case, the spectrum of photon emission acquires the finite width (line broadening) while the photon energy distribution becomes dependent also on the width η of the electron energy level E_v . Then the finite η causes an extra decoherence and broadening the THz laser emission spectrum. In a worst case scenario one can even get $\eta \geq \Delta$, which causes complete violating of the condition $E_v^T \equiv \Delta$. The latter example illustrates why creating the THz lasers is so difficult. Other sources of the T-beam decoherence and the line broadening consist of the temperature

fluctuations and noises which also strongly impact the THz device performance. Using graphene suggests several possible solutions of the mentioned decoherence problem. (i) One is able to form very narrow electron energy levels in the active region of the THz laser where $\eta \ll \Delta$. Very sharp and narrow e/h levels are obtained inside a narrow stripe of graphene with zigzag (ZZ) edges polarized by a transverse electric field as suggested in Refs. [4,33–36,42]. (ii) One can significantly reduce impact of phonons which essentially contribute into the level width η . It is accomplished when using a narrow stripe having a definite orientation in respect to crystallographic directions of the graphene lattice. The lattice symmetry and the atomic edges impose additional selection rules on the scattering probability involving just phonons with certain polarization and wave vector on one hand and electrons with one-dimensional dispersion law on the other hand. Such restriction rules out many inelastic scattering processes as irrelevant. Furthermore, due to narrow width δ of the electron bands in GQD, the high-energy phonons with frequency $f_{ph} > \delta/h$ do not participate in the electron-phonon scattering as well. The other mechanism involving the electron-electron collisions is less significant for graphene in the THz frequency range. The above results in very low energy dissipation in the graphene stripes with zigzag edges. (iii) The levels originate from the topologically protected edge states [35], hence they are robust in respect to the lattice imperfections and thermal excitations.

Here we consider the limit of high density of the charge carriers, whose energy recombination time τ_{HF} is much shorter than the change in polarization of the electromagnetic wave. The polarization relaxes very fast and is governed by the carrier-carrier and carrier-phonon scattering causing the relaxation to its quasiequilibrium value, which is determined by the momentary magnitudes of the field and the carrier density. This ensures the simplest *quasiequilibrium* conditions of a stationary excitation when the carriers are in equilibrium with themselves while the graphene stripe is out of equilibrium. In the quasiequilibrium approximation, the field intensity is a slow function of time. We disregard all the effects causing deviations from the quasiequilibrium assumption, such as spectral, spatial, or kinetic hole burning. This enables using the electron-hole-pair rate equation complemented with laser specific terms. The *rate equation* for generating of N photons takes the form

$$\dot{N} = r_p - r_{st} - r_{sp} - r_{nr}, \quad (15)$$

where r_p is the pumping rate, r_{st} is the stimulated emission rate, r_{sp} is the spontaneous emission rate, and r_{nr} is the nonradiative transitions rate. The *pump rate* due to injection current density j is $r_p = j\eta_{QE}/(eW)$ where η_{QE} is the quantum efficiency, and W is the transverse dimensions of the laser's active region (i.e., the stripe width). The *stimulated emission loss* rate is $r_{st} = -\chi''(\omega)\mathcal{E}_0^2/(2\hbar)$ where $\omega = 2\pi f$. The quasiequilibrium susceptibility $\chi(\omega)$ contains the factor $1 - f_{e,k} - f_{h,k} = (1 - f_{e,k})(1 - f_{h,k}) - f_{e,k}f_{h,k}$ that is conveniently separated in the two terms as $\chi''(\omega) = \chi_a''(\omega) - \chi_e''(\omega)$. Here $f_{e(h),k}$ is the distribution function of electron(hole)like HF excitations and the term $\chi_e''(\omega) \propto f_{e,k}f_{h,k}$ describes the emission while the other term $\chi_a''(\omega)$ describes the absorption, $\chi_a''(\omega) \propto (1 - f_{e,k})(1 - f_{h,k})$. The imaginary part of susceptibility $\chi_e''(\omega)$ is

related to the gain $g(\omega)$ as

$$g_e(\omega) = -\frac{4\pi}{n_b c} \omega \chi_e''(\omega), \quad (16)$$

where $g_e(\omega)$ is the probability per unit length to emitting a photon and the background refractive index is $n_b \simeq \sqrt{\epsilon_0}$. Thus $-g_e c/n_b$ is the emission probability of a photon per unit time. The *spontaneous emission* rate into the continuum of all photon modes with the frequency $\omega = \omega_{q,\lambda}$ where q, λ are the photon wave vector and polarization is

$$r_{sp} = \frac{4}{\pi \epsilon_0} \int dq q^2 \omega_q \chi_e''(\omega_q) \quad (17)$$

or

$$r_{sp} = \frac{1}{2\pi \epsilon_0} \int_0^\infty d\omega \left(\frac{2\omega n_b}{c} \right)^3 \chi_e''(\omega). \quad (18)$$

The dependence $\sim \omega^3$ indicates that the spontaneous emission losses dominate at higher laser frequencies. The *nonradiative* emission rate is computed as $r_{nr} = N/\tau + CN^3$ where the first term corresponds to the multiphoton emission involving deep trap levels while the second term might contain a significant contribution from the Auger processes in the THz lasers.

The T-ray laser emission is described in terms of the semiclassical electric field equation for spatial eigenmodes

$$[1 + 4\pi \chi(N)/\epsilon_0] \ddot{\mathcal{E}}_n + (\kappa c/n_b) \dot{\mathcal{E}}_n + \omega_n^2 \mathcal{E}_n = 0 \quad (19)$$

where ω_n is the eigenfrequency of the n th resonator mode and we have introduced the cavity loss rate as $\kappa c/n_b = 4\pi \sigma/\epsilon_0$ where σ is the electric conductivity. For Eq. (19), there are two regimes of the *steady state* solutions: (i) When the gain $g(\omega = 0)$ is less than the cavity losses, the laser field vanishes, i.e., for $\kappa > g(N_0, \omega_m)$ one gets the magnitude of time-averaged (i.e., at $\omega = 0$) electric field $\mathcal{E}_0 = 0$ and $r_p = N_0/\tau$, where N_0 is the time-averaged number of photons. (ii) If the gain becomes equal or exceeds the cavity losses provided $\kappa = g(N_0, \omega_m)$, one gets the finite magnitude of laser field, i.e., $\mathcal{E}_0 \neq 0$. Namely,

$$\mathcal{E}_0^2 = \frac{2\hbar}{\chi''(N_0)} \left(\frac{N_0}{\tau} - r_p \right) \quad (20)$$

and

$$\omega_m^2 = \frac{\omega_n^2}{1 + 4\pi \chi'(N_0)/\epsilon_0}, \quad (21)$$

where ω_m is the lasing frequency and χ' and χ'' are the real and imaginary parts of the optical susceptibility in the active region, ϵ_0 is the background dielectric constant. The above formula for ω_m^2 suggests that the pulling of the laser mode is caused by the refractive index changes due to the increased carrier density that is controlled by the gate voltages.

V. STEADY STATE SUSCEPTIBILITY OF GQD

Below we consider the effect of the electrochemical potential μ on the optical susceptibility of the graphene quantum dot (GQD), which is controlled by applying electric potentials to the back (or top) gate electrodes. The calculation results for the steady state optical susceptibility $\chi(\omega)$ are presented in Figs. 4, 5, 7, and 8.

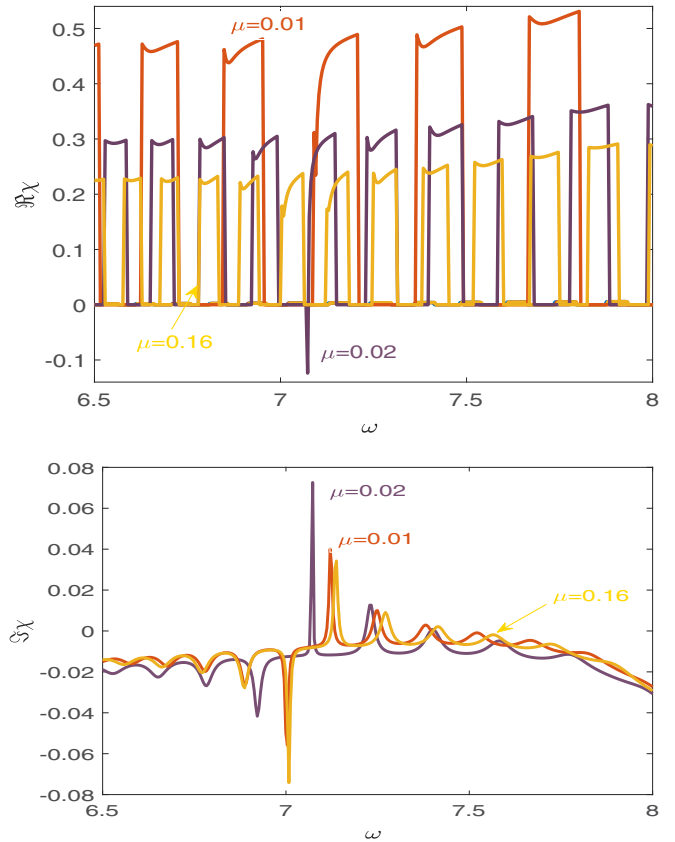


FIG. 4. The steady state optical susceptibility $\Re\chi(\omega)$ (top panel) and $\Im\chi(\omega)$ (bottom panel) as a function of frequency $\omega = 2\pi f$ in GQD computed for the stripe width $W = 2\hbar v_F/\Delta$, temperature $T = 1.4$ (in units of Δ/k_B , k_B is Boltzmann constant), the inelastic collision rate $\eta = 0.15$ and the level spacing (Stark splitting) $2\Delta = 2$ (all in units of Δ). Here $\omega = 2\pi f$, f is the frequency and μ is the electron electrochemical potential. The respective values of μ are shown in the figure.

The real $\Re\chi(\omega)$ and imaginary $\Im\chi(\omega)$ parts are shown in Fig. 4 as functions of frequency $\omega = 2\pi f$ for different values of the electrochemical potential μ , whose respective values are indicated in the figures. One can see that the frequency dependence of $\chi(\omega)$ dramatically changes as μ varies. Physically, this reflects the drastic change of the GQD optical properties since the magnitude of μ determines the quantization conditions at the graphene stripe edges. Remarkably, as μ changes, the signs and magnitudes of the real and imaginary parts of $\chi(\omega)$ alter. In Fig. 5, we detail the instability regions in the narrower frequency intervals. One can see that in certain frequency intervals the real part vanishes, $\Re\chi(\omega) = 0$, while $\Im\chi(\omega) < 0$ remains negative. An important conclusion drawn from Figs. 4 and 5 is that there is a set of resonant frequencies Ω_p determined by the condition $\Re\chi(\omega)|_{\omega=\Omega_p} = 0$ provided $\Im\chi(\omega) < 0$. Remarkably, the Ω_p magnitude depends on μ and Δ , so in experiments it can be controlled by applying appropriate electric potentials to the gate electrodes. Hence, based on the data presented in Figs. 4 and 5, one concludes that lasing conditions are fulfilled for $6.93 < \omega < 7.03$, $6.96 < \omega < 7.09$ and $7.14 < \omega < 7.22$ (in units of Δ). However, when $\Im\chi(\omega)$ becomes positive [see peaks of $\Im\chi(\omega)$ in Fig. 5], the lasing condition fails.

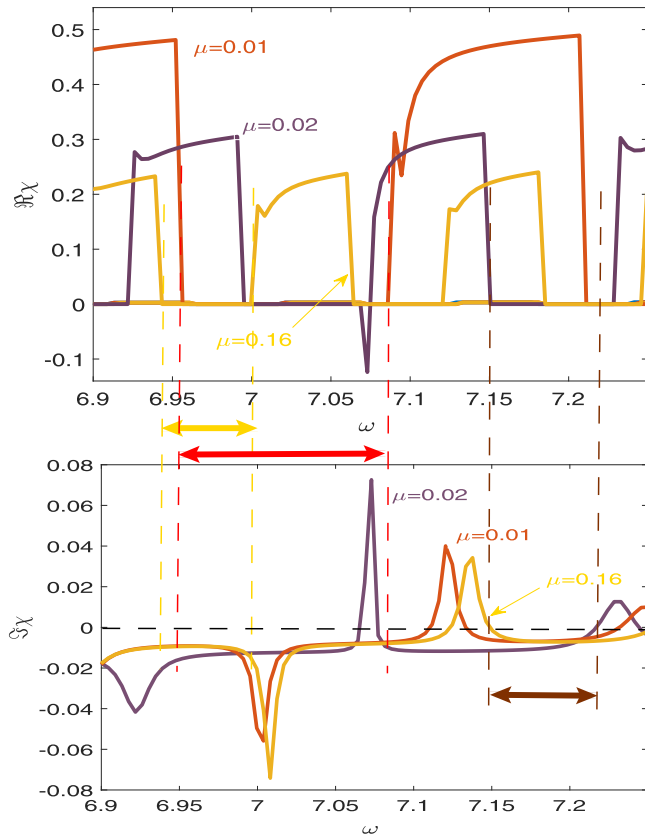


FIG. 5. Blowup $\Re\chi(\omega)$ (top panel) and $\Im\chi(\omega)$ (bottom panel) shown in the former Fig. 4 in the narrower frequency interval. The instability regions corresponding to the conditions $\Re\chi(\omega)|_{\omega=\Omega_p} = 0$ provided $\Im\chi(\omega) < 0$ are marked by arrows (the arrow colors correspond to the curve colors). They correspond to a set of resonant frequencies Ω_p determined by the mentioned conditions.

At first sight it seems there is a problem with generating the coherent THz radiation with the resonant frequency $\Omega_p \sim 6\Delta/\hbar$ when $\Omega_p < 3$ THz, which requires the minimum level spacing $\Delta < 3$ THz/6 = 0.5 THz. Such narrow level spacing ~ 2 meV corresponds to $k_B T \sim 20$ K, which is far below the room temperature $T_{\text{room}} \sim 300$ K. Deceptively, it seems that at $T = T_{\text{room}} \sim 300$ K, the large temperature broadening $\eta \sim 30$ meV smears the spectral singularities at $\epsilon = \pm\Delta$ out because it largely exceeds the level spacing $2\Delta = 4$ meV, thereby making the levels nondistinguishable. However, according to detailed calculations (see e.g., Ref. [43]) for the narrow levels in the graphene stripes with zigzag edges, the actual level broadening due to the inelastic scattering is two orders of magnitude lower than for conventional electrons with continuous dispersion law. The physical reason is that the localized HF excitations interact with phonons very weakly, because the respective phase space is confined. Therefore, the actual broadening of the (\pm) levels is very low and is below 3 meV even at $T = T_{\text{room}} \sim 300$ K. Thus, for narrower separation down to $2\Delta \sim 3$ meV in GQD that corresponds to $f \sim 0.7$ THz, the levels remain well defined even at room temperature.

To further illustrate the capability of the graphene quantum dot to forming the favorable lasing conditions we plot the

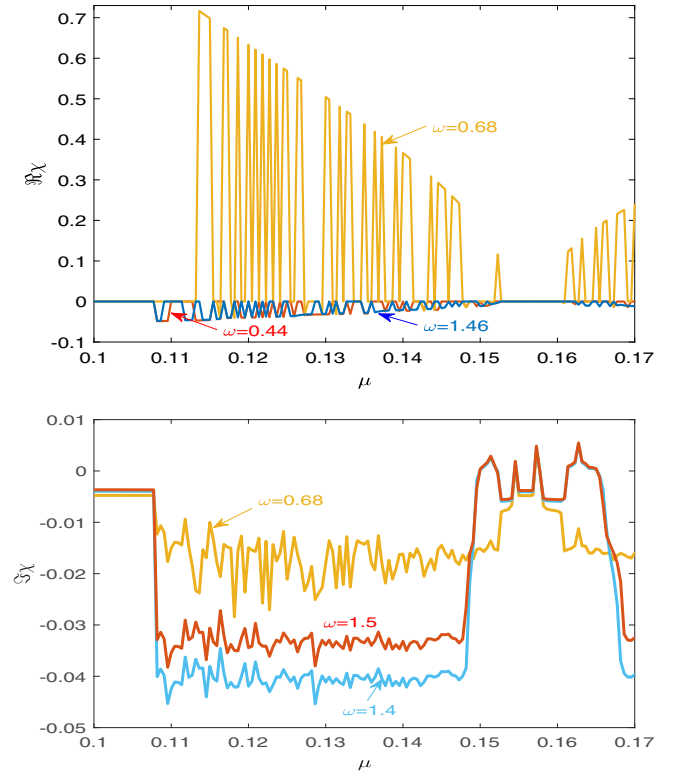


FIG. 6. The steady state susceptibility $\Re\chi(\mu)$ (top panel) and $\Im\chi(\mu)$ (bottom panel) as a function of electrochemical potential μ . The other parameters of GQD are the same as in Fig. 4. The respective values of ω are shown in the figure. Physically, the sharp switching occurs when μ hits the quantized level positions, which are dense for the relatively broad stripe.

dependencies $\Re\{\chi(\mu)\}$ and $\Im\{\chi(\mu)\}$ on the electrochemical potential μ in Fig. 6. From Fig. 6 one can see that by changing μ , one alters the shape of the susceptibility curves $\chi(\mu)$ considerably, thereby enabling the flexible control over the coherent T-ray emission. Furthermore, the fast switchings of $\Re\{\chi(\mu)\}$ and $\Im\{\chi(\mu)\}$ take place when μ hits the quantized level positions, which have narrow spacing and are dense for the relatively broad stripe $W = 2\hbar v_F/\Delta$. The gain versus frequency is shown in Fig. 7 (top panel). We also present a more detailed plot in a narrower frequency region Fig. 7 (bottom panel). From this Fig. 7 one can see that for the listed GQD parameters (i.e., the stripe width $W = 2\hbar v_F/\Delta$, temperature $T = 1.4\Delta/k_B$, the inelastic collision rate $\eta = 0.15\Delta$ and the Stark splitting 2Δ), the gain exceeds the cavity loss. Provided $\Re\{\chi(\omega, \mu)\} \sim 0$, which is the case in certain intervals of μ , one achieves the necessary conditions for the coherent T-ray emission.

A general insight into the sign switching of the optical susceptibility for the graphene quantum dot versus ω and μ is given in the contour plot of $\Im\chi(\omega, \mu)$ as shown in Fig. 8 (top panel) where the green regions correspond to $\Im\chi < 0$ while yellow areas to $\Im\chi > 0$. Interestingly, the sign switch does not happen for much narrower stripes with $W = 0.2\hbar v_F/\Delta$ where the level spacing is wide, although the whole dependence $\Im\chi(\omega, \mu)$ becomes much smoother as shown in Fig. 8 (bottom panel).

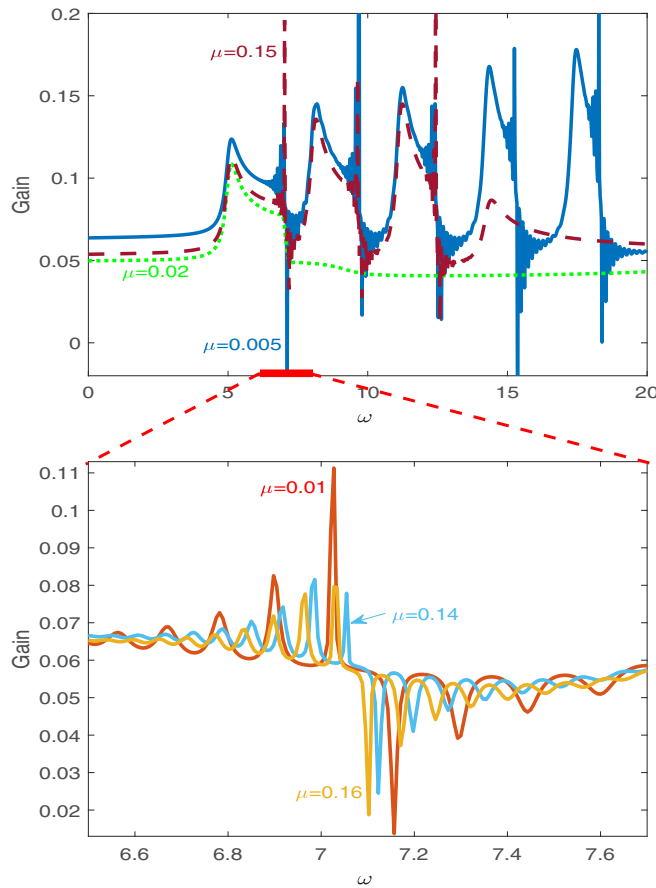


FIG. 7. Top panel: Gain as a function of frequency $\omega = 2\pi f$ in GQD computed for the stripe width $W = 2\hbar v_F/\Delta$, temperature $T = 1.3\Delta/k_B$, the inelastic collision rate $\eta = 0.15\Delta$, the level spacing (Stark splitting) 2Δ , and the ac field amplitude $E_{ac}^{(0)} = 2.3\Delta/eW$. The respective values of electrochemical potential μ inside the active region are shown in the figure. Bottom panel: Blowup of the frequency region denoted by red in the top panel that detail the fine structure of the gain function near the lowest resonant frequency.

When designing the graphene THz lasers, there are other potential issues as follows. (a) Pumping of nonequilibrium electron and hole excitations into the active region of the THz laser causes not only inverse population of the e/h levels. An adverse side effect is that the nonequilibrium electrons and holes eventually transfer their excessive energy to the lattice oscillations and to other excitations in the system. This leads to an overall heating of the active region during the induced emission process. Excessive Joule heating of the active region might change its properties and can even adversely impact the overall performance of the THz laser. Therefore, one should pay attention to reducing the unwanted heating. The adverse heating can be diminished by implementing the active region with an appropriate geometry, crystallographic orientation, and dimensions. In this way one eliminates certain electron-phonon scattering processes, e.g., by using a stripe-shaped active region with zigzag edges. Similarly, one excludes the indirect interlevel transitions which cause the acoustic phonon emission. The remaining contribution originates solely from the direct interlevel electron-hole recombination processes providing emission of the THz photons out of the active

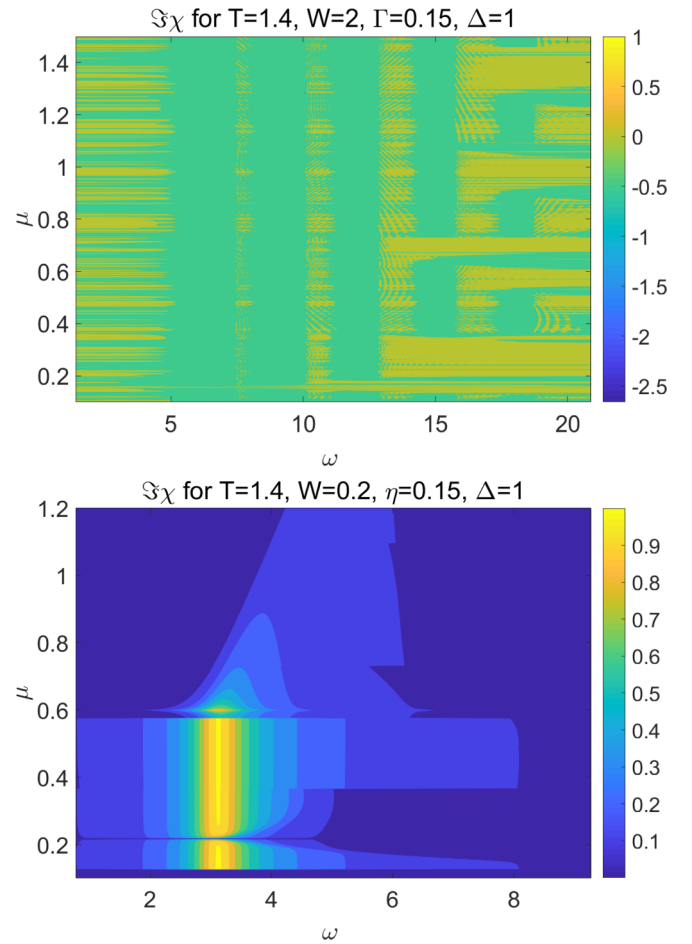


FIG. 8. Top panel: Contour plot illustrating the sign switching of $\Im\chi(\mu, \omega)$ for the graphene quantum dot versus the frequency ω and electrochemical potential μ (both in units of Δ) on the larger scale. Here the green regions correspond to $\Im\chi < 0$ while yellow areas to $\Im\chi > 0$. The GQD parameters are the same as in Fig. 7. Bottom panel: Contour plot $\Im\chi(\mu, \omega)$ for much narrower stripe $W = 0.2\hbar v_F/\Delta$. The dependence is much smoother but the sign does not change.

region. (b) Forming an optimal energy spectrum inside the active region. An increased width of the electron energy levels restricts the device performance, widens overall frequency interval, and causes line broadening of the generated T beam. One solution is to design an active region with narrow ($\eta \ll \Delta$) quantized energy levels. It can be accomplished by placing the appropriate split gates right on the top of the graphene sheet [see Fig. 2(a)]. An example of the energy diagram of the gate/open graphene region boundary is sketched in Fig. 2(b). The electric potential penetrates from the gate region into the open graphene on the Debye screening length 0.5–2 nm, depending on the temperature and the charge carrier concentration. Figures 2(c) and 2(d) show the electron subband structure and the local electron density of states in the active region, respectively. (c) A distinguished feature of graphene is anisotropy of the microscopic transport. Therefore one should design the active region with appropriate dimensions and orientation. In this way, the major THz laser parameters can be well defined during the fabrication process.

There are several reasons why the graphene THz lasers have a remarkable potential as compared to their conventional semiconducting counterparts. (i) The intrinsic coherence in graphene is preserved far better than in other nonsuperconducting electronic materials. It happens due to so-called pseudospin conservation which is an intrinsic feature of graphene. In particular, the good intrinsic coherence helps to reduce the intrinsic noises. (ii) The energy relaxation in graphene is typically much slower than in other conductors. It allows achieving a considerable degree for the inverse level population. (iii) Technically, the energy dependence of the election density of states in the 2D graphene enables manipulating of their properties by mere applying electric potentials to the gate electrodes. Furthermore, the 2D geometry is well suited to fabricating the bottom, top, and side gate electrodes. Owing to (i)–(iii), GQD comprises a system with the robust, voltage-controlled narrow quantized energy levels, a considerable inverse level population, good accumulation of the pumped energy, which generates a very strong THz monochromatic beam.

The dissipative processes inside the active region cause fluctuations that can be approximately described in terms of the quantum mechanical Langevin equations. In this way one finds that the noise terms due to spontaneous emission is $\propto r_{sp}$ and the nonradiative transition noise is $\propto r_{nr}$.

VI. NONLINEAR ELECTROMAGNETIC PROPERTIES OF GQD

The unconventional excitation spectrum of the chiral fermions in the graphene stripe results in nonlinear electromagnetic properties of the two-dimensional atomic monolayer material. In particular, graphene has remarkable nonlinear properties in the terahertz (THz) frequency range. These create many suggestions for novel photonic devices, such as THz devices [44], optical modulators [45], photodetectors [46], and polarizers [47]. One promising direction is exploiting the nonlinear electromagnetic response of the graphene stripe to an ac electromagnetic field. Such a nonlinear effect might be used for the frequency multiplication or for self-focusing of two dimensional Townes-like solitons in the electrically tunable metastructure shown in Fig. 1. Doping graphene by applying the electric potentials to the gate electrodes allows fine tuning the nonlinear properties of the metastructure. Total internal reflection at the boundaries of the dielectric waveguide causes the confinement of the E field along the lateral x direction. As the y coordinate is varied along the stripe axis, the normalized E field cross section along the x direction changes. Such change, which is larger than in planar nonlinear waveguides, corresponds to a significant nonlinear optical current supported by the 2D graphene stripe. Below we find that the third-order susceptibility in the graphene stripe is large enabling us to form the TE and TM spatial solitons. Stable Townes-like spatial solitary waves propagating in the longitudinal direction originate from the intraband current dominating the electron dynamics for THz excitations of doped graphene. Significant magnitudes of the nonlinear optical susceptibilities in the 2D graphene sheets were theoretically predicted in Refs. [8,9]. They have been

experimentally observed for third-order nonlinear effects by the authors of Ref. [10].

A nonlinear effect utilized to control light propagation at the micro- and nanoscales is the formation of temporal and spatial EM solitons [11]. We analyze the respective nonlinear contribution for the graphene strip in the geometry shown in Fig. 1. Consider a classical 2D particle with the charge $-e$ and the energy spectrum (4), (5) as for a chiral fermion in the graphene stripe with zigzag edges exposed to the time-dependent harmonic y -polarized electric field $E_{ac}(t) = E_{ac}^0 \cos \Omega t$. The relevant excitations are electrons in the vicinity of one gap edge while taking into account the presence of two nonequivalent gap regions in the Brillouin zone by introducing the valley-degeneracy factor $g_v = 2$. According to the Newton equation of motion

$$\frac{dk_y}{dt} = -\frac{e}{\hbar} E_{ac}(t) \quad (22)$$

where we assume that the ac field is polarized along the stripe y axis. In Eq. (22), the momentum $k_y(t)$ is given by

$$k_y(t) = k_0(t) = \varepsilon \sin \Omega t, \quad (23)$$

where $\varepsilon = eE_{ac}^0/\hbar\Omega$.

In conventional 2D electron systems with the parabolic energy dispersion, the velocity v_y , and hence, the current $j_y = -en_s v_y$ are proportional to $\hbar k_y$, so that the normal 2D system responds at the same frequency where n_s is the areal density of charge carriers. This is different for the graphene stripe where the velocity

$$\begin{aligned} v_y &= \frac{1}{\hbar} \frac{\partial E_p}{\partial k_y} \\ &= v_F \frac{k_y}{\sqrt{k_x^2 + k_y^2(t) + (\Delta/v_F)^2}} \\ &= v_F \frac{\varepsilon \sin \Omega t}{\sqrt{k_x^2 + \varepsilon^2 \sin^2 \Omega t + (\Delta/v_F)^2}} \end{aligned} \quad (24)$$

is not merely proportional to k_y . In the extreme limit, when k_x and Δ/v_F in Eq. (24) are close to zero, v_y is proportional to $\text{sgn}(p_x)$ and the ac electric current $j_y = -en_s v_y$ has anharmonic contributions

$$j_y(t) = en_s v_F \frac{4}{\pi} \left\{ \sin \Omega t + \frac{1}{3} \sin 3\Omega t + \frac{1}{5} \sin 5\Omega t + \dots \right\}. \quad (25)$$

Both the gate voltage and chemical doping can shift the chemical potential μ of electrons in graphene to the upper E_{p2} or to the lower E_{p1} band. Let us assume that the chemical potential μ lies in the upper band $E_{p2} = v_F p$, the temperature is small, $k_B T \ll \mu$, and the system is subjected to the time-dependent ac electric field $E_{ac}(t)$. Then the momentum distribution function of electrons $f_p(t)$ is described [8] by Boltzmann equation

$$\frac{\partial f_p(t)}{\partial t} - \frac{\partial f_p(t)}{\partial \mathbf{p}} \cdot e \mathbf{E}_{ac}(t) = 0, \quad (26)$$

where we have disregarded collisions of electrons with impurities, phonons, and other lattice imperfections. Equation

(26) has the exact solution

$$f_p(t) = \mathcal{F}_0(\mathbf{p} - \mathbf{p}_0(t)), \quad (27)$$

where

$$\mathcal{F}_0(\mathbf{p}) = \frac{1}{\exp\left(\frac{v_F p - \mu}{T}\right) + 1} \quad (28)$$

is the Fermi-Dirac function, and

$$\mathbf{p}_0(t) = -e \int_{-\infty}^t dt' \mathbf{E}_{ac}(t') \quad (29)$$

is the solution of the single particle classical equation of motion. Thus, the former equations derived in previous sections remain valid provided we replace $\mathbf{p} \rightarrow \mathbf{p} - \mathbf{p}_0(t)$ in the respective distribution functions.

The nonlinear regime (25) is achieved at $|p_0| \gg p_F$, or at

$$\mathcal{E} \equiv \frac{eE_{ac}^0 v_F}{\Omega \mu} \gg 1. \quad (30)$$

According to Eq. (30), the nonlinear effect becomes essential already at $E_{ac}^0 \geq 1.4$ kV/cm provided $f = \Omega/2\pi = 1$ THz and $\mu = 0.06$ eV. The meaning of the above relationship (30) is that the energy, gained by electrons from the ac field during the oscillation period, should be large as compared to their average equilibrium energy. In the low-field limit, the response is linear [i.e., the $j(t)$ dependence has a sinusoidal form], while at strong fields the time dependence of the current tends to that given by Eq. (25). The strong-field condition (30) can be rewritten as

$$E_{ac}^0 \gg \frac{2\Omega\sqrt{\pi n_s}}{e\sqrt{g_s g_v}} \quad (31)$$

which means that the required ac electric field grows linearly with the electromagnetic wave frequency and with the square root of the electron density.

There are following limitations on applicability of the quasiclassical method to describing the electromagnetic response of graphene stripe. Physically, using the Newton equation (22), one takes into account contribution the intraband transitions to the ac electric current while ignoring the interband transitions between the lower quasihole and the upper quasihole bands. This is only possible if the frequency of the electromagnetic radiation satisfies the inequality

$$\Omega \ll \max\{\mu, T\}. \quad (32)$$

At room temperature and for the electric charge carrier densities $n_s \simeq 10^{11}-10^{12}$ cm⁻² the above inequality limits the frequency band to $\sim 10-30$ THz.

We estimate the third-order susceptibility $\chi_{gr}^{(3)}$ by computing the relevant Fourier coefficients of the time-dependent $\chi(t, \mathbf{E}_{ext}(t))$ as

$$\chi_{gr}^{(n)}(\Omega, \mathbf{E}_{ext}^0) = \frac{\Omega}{2\pi} \int_0^{2\pi/\Omega} \chi(t', \mathbf{E}_{ext}(t')) e^{-i\Omega n t'} dt', \quad (33)$$

where Ω is the ac field frequency, n is the integer number. Likewise, we also expand the electric current density in graphene stripe j_{gr} in powers of $\psi = eA/p_F$ (where A is the

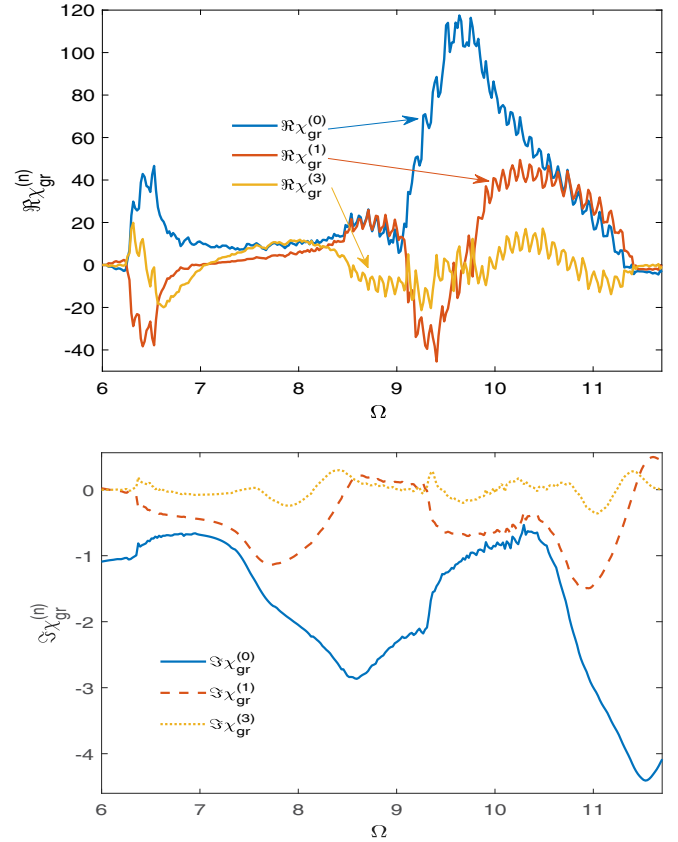


FIG. 9. Top panel: The $\Re\chi_{gr}^{(n)}(\Omega, \mathbf{E}_{ext}^0)$ for the harmonics $n = 0, 1, 3$ as functions of the ac field frequency Ω . The GQD parameters are as follows: The stripe width $W = 2\hbar v_F/\Delta$, temperature $T = 1.2\Delta/k_B$, the inelastic collision rate $\eta = 0.12\Delta$, the level spacing (Stark splitting) 2Δ , and the ac field amplitude $E_{ac}^0 = 2.3\Delta/eW$. Bottom panel: Respective plots for $\Im\chi_{gr}^{(n)}(\Omega, \mathbf{E}_{ext}^0)$. One can see that the magnitudes of all the harmonics are comparable with each other.

vector potential) up to the third order:

$$j_{gr} \simeq \frac{\psi}{\sqrt{1+\psi^2}} \simeq \psi - \frac{\psi^3}{8}, \quad (34)$$

finding the nonlinear third order intraband current density $j_{gr}^{(3)}$.

Harmonics of the ac field-dependent nonlinear susceptibility $\chi_{gr}^{(n)}(\Omega, \mathbf{E}_{ext}^0)$ are computed numerically using the above formulas. In Fig. 9 we show the Fourier components of the current versus the field parameter \mathcal{E} given by Eq. (30). When \mathcal{E} becomes larger than $\simeq 4$, the Fourier amplitudes saturate and one gets in the ultimate nonlinear regime. From the plots of susceptibility harmonics $\Re\chi_{gr}^{(0,1,3)}(\Omega, \mathbf{E}_{ext}^0)$ and $\Im\chi_{gr}^{(0,1,3)}(\Omega, \mathbf{E}_{ext}^0)$ illustrating the nonlinear effects in graphene stripe with zigzag edges shown in Fig. 9 one can see that the zeroth, first, and third harmonics of $\chi(t', \mathbf{E}_{ext}(t'))$ are about the same order of magnitude, which suggests the significance of nonlinear phenomenon in the GQD system under consideration. In conclusion of this section, due to the unconventional dispersion law (4), (5) of the chiral fermions, the response of graphene stripe to an ac electromagnetic field is intrinsically nonlinear.

VII. TIME EVOLUTION OF SUSCEPTIBILITY

An accurate estimation of the time required to reach the steady state regime represents a tedious task involving a self-consistent solution of a complex system of the Boltzmann equations complemented by equations for the HF excitation spectrum. Besides, the equations must be complemented by respective boundary conditions defining the geometry and initial state. In this work we provide just the simplest insight into how the optical susceptibility $\chi''(\omega, t)$ evolves in response to a pulse of injection current incurring a sharp change of the effective electron temperature T^* of GQD. Let us assume that the pulse of injection current heats GQD, whose effective temperature increases up to T^* . Basically, after the pulse ends, the time evolution of the HF distribution function $f(\epsilon, t)$ is found as a solution of the Boltzmann equation. For the sake of simplicity, we use the effective temperature approximation that gives

$$f(\epsilon, t) = \frac{1}{\exp\left(\frac{\epsilon - \mu}{T^*(t)}\right) + 1}, \quad (35)$$

where the time dependence of T^* is determined by the energy relaxation of the HF distribution function. In the above approximation we use

$$T^*(t) = T \exp\left[\left(-\frac{t - t_0}{\tau_p}\right)^n\right], \quad (36)$$

where we take $n = 100$ and $t_0 = \tau_p = 2.5$ ns. When the energy recombination time τ_{HF} of the HF excitations is very short, $\tau_{\text{HF}} \ll \min\{\tau_p, t_0\}$ (typically $\tau_{\text{HF}} \sim 10^{-12}$ s), the time evolution of $T^*(t)$ immediately follows the change of injection current, $T^*(t) \propto j(t)$. However, the scenario becomes different when $\tau_{\text{HF}} \sim \{\tau_p, t_0\}$. In the last case, when the injection current pulses are sufficiently short, the optical susceptibility reaches the steady state on the timescale $\sim \tau_{\text{HF}}$. Such time evolution of $\Im\chi(\omega, t)$ is illustrated in Fig. 10 by using the above simple model (35) and (36) allowing us to determine the behavior of the graphene ‘‘particle’’ from the time that the injection current pulse ends ($t = 0$ ps) until reaching steady state at $t = 2$ ps. The graph in Fig. 10 helps us to understand and evaluate the role of nonequilibrium effect in GQD.

VIII. CONCLUSIONS

Obtained results suggest that the considered design of the graphene quantum dot (GQD) allows the all-electrical control of the optical susceptibility $\chi(\omega, \mu)$. This becomes possible because the magnitude and sign of both the real and imaginary parts of $\chi(\omega, \mu)$ depend on the electrochemical potential μ and on the frequency variable ω . Technically, in the GQD structure one can change the magnitudes of Δ and μ by applying appropriate electric potentials to the local gates as depicted in Fig. 1, thereby enabling the flexible control of the GQD optical properties.

Furthermore, like the pristine graphene, the GQD structure has remarkable nonlinear electromagnetic properties stemming from the unconventional dispersion law of the chiral fermions in the graphene stripe with zigzag edges. A strong nonlinear effect arises because the optical susceptibility depends on the ac field intensity. The magnitude of high-order

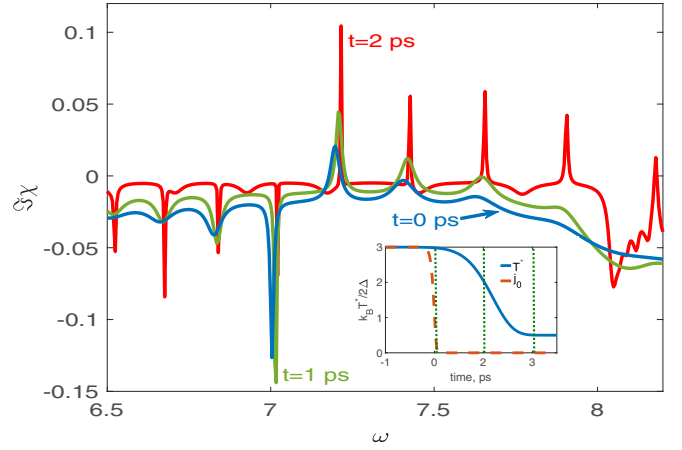


FIG. 10. The imaginary part of optical susceptibility $\Im\chi(\omega, t)$ as functions of the frequency ω at time moments $t = 0$ ps, 1 ps, and 2 ps after the injection current pulse ends. Here we used the GQD stripe width $W = 2h\nu_F/\Delta$, the steady state temperature $T = 0.5\Delta/k_B$, the level spacing (Stark splitting) 2Δ , and the energy relaxation time $\tau_{\text{HF}} = 1$ ps. One can see that the steady state of GQD is achieved at $t \sim 2$ ps, after the injection current pulse ends and the HF excitations recombine in the energy. Inset shows the time dependence of the effective temperature $T^*(t)$ (solid blue line) that achieves its steady state value $T = 0.5\Delta/k_B$ at $t \sim 2$ ps, after the injection current pulse (red dash) ends at $t = 0$.

harmonics is significant even in relatively weak ac fields, causing the appearance of a variety of the nonlinear effects.

In experiments, the THz radiation is detected in several ways. For instance, one can form a Josephson junction in an adjacent area on the same substrate, which will serve as a THz detector. Another option is to deposit a GQD THz detector on the same substrate next to the GQD THz emitter. Furthermore, one can use metallic co-planar strip lines as THz antennas to detect the THz rays. Special attention must be paid to creating the sharp and narrow electron quantized levels formed between two timberlike multilayered gate electrodes deposited along the ZZ direction. The energy levels are robust in the presence of lattice defects and imperfections remaining are very narrow and sharp since they are topologically protected [4,35,42]. In the active region of the THz emitter, the coherent monochromatic THz waves originate from the quantum transitions between the sharp localized levels. The energy level splitting is readily controlled by the voltage difference between the gate electrodes having a multilayered structure as depicted in Fig. 1.

The unconventional electromagnetic (EM) properties of the graphene quantum dots (GQD) have a promising potential for practical applications. Experimentally, it would be interesting to fabricate the all-electrically controlled GQD based on the graphene stripes with atomic zigzag edges. The calculation results of the optical susceptibility indicate strong dependence on the frequency and electrochemical potential, which can be exploited for experimental observing of the tunable THz emission. Another result is the nonlinear electromagnetic response of GQD, whose mechanism is related to the unconventional properties of chiral fermions in graphene stripes with atomic zigzag edges. The obtained data allow

better understanding of the physical mechanisms related to the electrically controlled GQD showing remarkable electromagnetic properties.

APPENDIX: APPENDIX

Susceptibility of pristine graphene

Here we provide technical details concerning the optical susceptibility of pristine graphene. We use Eq. (1), which is written for indirect interband transitions accompanied by the absorption/emission of a phonon with the finite momentum $\mathbf{q} \neq \mathbf{0}$. Here we use units with $\hbar = 1$ and $k_B = 1$ if not stated otherwise. When the absorption/emission process is accompanied by the photon instead of the phonon, the interband transitions become direct and the above Eq. (1) is simplified. For the photons, whose absorption creates the electronlike HF (below for brevity we call them electrons) in the conductive band while the holelike HF (we call them holes) in the valence band (direct interband transitions), we set $\mathbf{q} = \mathbf{0}$. Then, using $ss' = -1$ we get the respective energy change as $\epsilon_{s',v} - \epsilon_{s,c} = \pm 2\epsilon$ and from Eq. (1) we get

$$\chi(\omega) = -\frac{6\sqrt{3}|d_{cv}|^2}{\pi v_F^2} \int_0^{v_F\Lambda} d\epsilon \epsilon (f(-\epsilon) - f(\epsilon)) \quad (\text{A1})$$

$$\times \left(\frac{1}{\omega + 2\epsilon + i\eta} - \frac{1}{\omega - 2\epsilon + i\eta} \right), \quad (\text{A2})$$

where $\Lambda \approx 1/a$ is the cutoff momentum and a is the lattice constant.

In the beginning we find how the steady state functions $\chi(\omega)$ and $\chi(\mu)$ depend, respectively, on the photon frequency ω and the HF electrochemical potential μ . In the above formulas we set

$$f(\epsilon) = \frac{1}{e^{(\epsilon-\mu)/T} + 1}. \quad (\text{A3})$$

In the zero-temperature limit $T = 0$ we simply set $f(\epsilon) = \theta(\mu - \epsilon)$ and $f(-\epsilon) = 1$ for electron doping with $\mu > 0$, where μ is the electron electrochemical potential. Respectively, for the hole doping we get $\mu < 0$. Then

$$\chi(\omega) = -\frac{6\sqrt{3}|d_{cv}|^2}{\pi v_F^2} \int_{\mu}^{v_F\Lambda} \times \left(\frac{1}{\omega + 2\epsilon + i\eta} - \frac{1}{\omega - 2\epsilon + i\eta} \right) \epsilon d\epsilon, \quad (\text{A4})$$

where $\zeta^2 = (\eta^2 - 2i\eta\omega - \omega^2)/4$ and we have used

$$f(-\epsilon) - f(\epsilon) = 1 - \theta(\mu - \epsilon) = \begin{cases} 0 & \text{for } \epsilon < \mu \\ 1 & \text{for } \epsilon > \mu \end{cases}. \quad (\text{A5})$$

An immediate integration of Eq. (A4) gives a simple analytical expression in the form

$$\chi(\omega, \mu) = -\frac{i}{\pi} \frac{3\sqrt{3}|d_{cv}|^2}{2\pi v_F^2} \left[\Lambda - \mu + \frac{\omega + i\eta}{2} \times \left(\tanh^{-1} \left(\frac{2\mu}{\omega + i\eta} \right) - \tanh^{-1} \left(\frac{2\Lambda}{\omega + i\eta} \right) \right) \right]. \quad (\text{A6})$$

The above calculations are illustrated in Fig. 3 where we show the real $\chi' = \Re\chi$ and imaginary $\chi'' = \Im\chi$ parts of the optical susceptibility versus the frequency ω and electrochemical potential μ .

$$\chi(\omega, \mu) = -\frac{6\sqrt{3}|d_{cv}|^2}{\pi v_F^2} \left[v_F\Lambda - \mu + \frac{\omega}{4} \times \left(\ln \left| \frac{\omega + 2\mu}{\omega - 2\mu} \right| + i\pi\theta(\omega - 2\mu) \right) \right]. \quad (\text{A7})$$

It is also instructive to find the number of excitations $n(\mu)$ in the 2D graphene. For the equilibrium case we find

$$\begin{aligned} n &= \frac{N}{L^2} = -\frac{12\sqrt{3}}{\pi v_F^2} \int_0^{v_F\Lambda} \epsilon f(\epsilon) d\epsilon \\ &= -\frac{12\sqrt{3}}{\pi v_F^2} \int_0^{v_F\Lambda} \epsilon \frac{1}{e^{\beta(\epsilon-\mu)} + 1} d\epsilon \\ &\quad - \frac{12\sqrt{3}}{\pi v_F^2 \beta^2} \int_0^{\beta v_F\Lambda} \epsilon \frac{1}{e^{\epsilon-\beta\mu} + 1} d\epsilon. \end{aligned}$$

Then one gets

$$\begin{aligned} n(\mu) &= -(12\sqrt{3}T^2/\pi v_F^2) [Li_2(-e^{-\frac{\mu}{T}}) - Li_2(-e^{-\frac{\Lambda-\mu}{T}}) \\ &\quad + \Lambda(\Lambda - 2T \log(e^{-\frac{\Lambda-\mu}{T}} + 1))/T^2]. \end{aligned} \quad (\text{A8})$$

In more realistic conditions, e.g., when the temperature is finite while the graphene sheet is deposited on a substrate and its electronic states are controlled by gate electrodes, one finds the optical susceptibility numerically, as described in the main text. Likewise, numeric solutions are also used for studying the nonstationary and nonequilibrium properties of the graphene samples [48–52].

- [1] X. Liu, Z. Chen, E. P. J. Parrott, B. S. Y. Ung, J. Xu, and E. Pickwell-MacPherson, Graphene based terahertz light modulator in total internal reflection geometry, *Adv. Opt. Mater.* **5**, 1600697 (2017).
 [2] Z. Chen, X. Chen, L. Tao, K. Chen, M. Long, X. Liu, K. Yan, R. I. Stantchev, E. Pickwell-MacPherson, and J. B. Xu, Graphene controlled Brewster angle device for ultra broadband terahertz modulation, *Nat. Commun.* **9**, 4909 (2018).

- [3] T. Low, A. Chaves, J. D. Caldwell, A. Kumar, N. X. Fang, P. Avouris, T. F. Heinz, F. Guinea, L. Martin-Moreno, and F. Koppens, Polaritons in layered two-dimensional materials, *Nat. Mater.* **16**, 182 (2017).
 [4] S. Shafraniuk, *Thermoelectricity and Heat Transport in Graphene and Other 2D Nanomaterials* (Elsevier, Amsterdam, 2016).
 [5] S. E. M. Rinzan, G. Jenkins, H. D. Drew, S. Shafranjuk, and P. Barbara, Carbon nanotube quantum dots as highly

- sensitive terahertz-cooled spectrometers, *Nano Lett.* **12**, 3097 (2012).
- [6] T. Fuse, Y. Kawano, T. Yamaguchi, Y. Aoyagi, and K. Ishibashi, Quantum response of carbon nanotube quantum dots to terahertz wave irradiation, *Nanotechnology* **18**, 044001 (2007).
- [7] S. Chakraborty, O. P. Marshall, T. G. Folland, Y.-J. Kim, A. N. Grigorenko, and K. S. Novoselov, Gain modulation by graphene plasmons in aperiodic lattice lasers, *Science* **351**, 246 (2016).
- [8] S. A. Mikhailov, Non-linear electromagnetic response of graphene, *Europhys. Lett.* **79**, 27002 (2007).
- [9] K. L. Ishikawa, Nonlinear optical response of graphene in time domain, *Phys. Rev. B* **82**, 201402(R) (2010).
- [10] E. Hendry, P. Hale, J. Moger, A. Savchenko, and S. Mikhailov, Coherent Nonlinear Optical Response of Graphene, *Phys. Rev. Lett.* **105**, 097401 (2010).
- [11] R. W. Boyd, *Nonlinear Optics* (Academic Press, New York, 1992).
- [12] L. Ju, B. Geng, J. Horn, C. Girit, M. Martin, Z. Hao, H. A. Bechtel, X. Liang, A. Zettl, Y. Ron Shen, and F. Wang, Graphene plasmonics for tunable terahertz metamaterials, *Nat. Nanotechnol.* **6**, 630 (2011).
- [13] T. Eberlein, U. Bangert, R. R. Nair, R. Jones, M. Gass, A. L. Bleloch, K. S. Novoselov, A. Geim, and P. R. Briddon, Plasmon spectroscopy of free-standing graphene films, *Phys. Rev. B* **77**, 233406 (2008).
- [14] J. T. Kim and S.-Y. Choi, Graphene-based plasmonic waveguides for photonic integrated circuits, *Opt. Express* **19**, 24557 (2011).
- [15] J. Chen, M. Badioli, P. Alonso-González, S. Thongrattanasiri, F. Huth, J. Osmond, M. Spasenović, A. Centeno, A. Pesquera, P. Godignon, A. Z. Elorza, N. Camara, F. J. G. de Abajo, R. Hillenbrand, and F. H. Koppens, Optical nano-imaging of gate-tunable graphene plasmons, *Nature (London)* **487**, 77 (2012).
- [16] Z. Fei, A. S. Rodin, G. O. Andreev, W. Bao, A. S. McLeod, M. Wagner, L. M. Zhang, Z. Zhao, M. Thiemens, G. Dominguez, M. M. Fogler, A. H. Castro Neto, C. N. Lau, F. Keilmann, and D. N. Basov, Gate-tuning of graphene plasmons revealed by infrared nano-imaging, *Nature (London)* **487**, 82 (2012).
- [17] A. N. Grigorenko, M. Polini, and K. S. Novoselov, Graphene plasmonics, *Nat. Photon.* **6**, 749 (2012).
- [18] H. Yan, T. Low, W. Zhu, Y. Wu, M. Freitag, X. Li, F. Guinea, P. Avouris, and F. Xia, Damping pathways of mid-infrared plasmons in graphene nanostructures, *Nat. Photon.* **7**, 394 (2013).
- [19] X. Wang, Z. Cheng, K. Xu, H. K. Tsang, and J.-B. Xu, High-responsivity graphene/silicon-heterostructure waveguide photodetectors, *Nat. Photon.* **7**, 888 (2013).
- [20] E. O. Polat and C. Kocabas, Broadband optical modulators based on graphene supercapacitors, *Nano Lett.* **13**, 5851 (2013).
- [21] K. S. Novoselov, V. I. Fal'ko, L. Colombo, P. R. Gellert, M. G. Schwab, and K. Kim, A roadmap for graphene, *Nature (London)* **490**, 192 (2012).
- [22] W. L. Barnes, A. Dereux, and T. W. Ebbesen, Surface plasmon subwavelength optics, *Nature (London)* **424**, 824 (2008).
- [23] E. Ozbay, Plasmonics: Merging photonics and electronics at nanoscale dimensions, *Science* **311**, 189 (2006).
- [24] C. J. Docherty, C.-T. Lin, H. J. Joyce, R. J. Nicholas, L. M. Herz, L.-J. Li, and M. B. Johnston, Extreme sensitivity of graphene photoconductivity to environmental gases, *Nat. Commun.* **3**, 1228 (2012).
- [25] A. Das, S. Pisana, B. Chakraborty, S. Piscanec, S. K. Saha, U. V. Waghmare, K. S. Novoselov, H. R. Krishnamurthy, A. K. Geim, A. C. Ferrari, and A. K. Sood, Monitoring dopants by Raman scattering in an electrochemically top-gated graphene transistor, *Nat. Nanotechnol.* **3**, 210 (2008).
- [26] F. Bonaccorso, Z. Sun, T. Hasan, and A. C. Ferrari, Graphene photonics and optoelectronics, *Nat. Photon.* **4**, 611 (2010).
- [27] A. Tredicucci and M. S. Vitiello, Device concepts for graphene-based terahertz photonics, *IEEE J. Sel. Top. Quantum Electron.* **20**, 130 (2014).
- [28] D. Bimberg, M. Grundmann, and N. N. Ledentsov, *Quantum Dot Heterostructures* (Wiley, New York, 1999).
- [29] D. Bimberg, M. Kuntz, and M. Laemmlin, Quantum dot photonic devices for lightwave communication, *Microelectronics Journal* **36**, 175 (2005).
- [30] D. Bimberg, Quantum dot based nanophotonics and nanoelectronics, *Electron. Lett.* **44**, 168 (2008).
- [31] Yu. V. Bludov, D. A. Smirnova, Yu. S. Kivshar, N. M. R. Peres, and M. I. Vasilevskiy, Nonlinear TE-polarized surface polaritons on graphene, *Phys. Rev. B* **89**, 035406 (2014).
- [32] P. Ruffieux, S. Wang, B. Yang, C. Sánchez-Sánchez, J. Liu, T. Dienel, L. Talirz, P. Shinde, C. A. Pignedoli, D. Passerone, T. Dumslaff, X. Feng, K. Müllen, and R. Fasel, On-surface synthesis of graphene nanoribbons with zigzag edge topology, *Nature (London)* **531**, 489 (2016).
- [33] L. Brey and H. A. Fertig, Edge states and the quantized Hall effect in graphene, *Phys. Rev. B* **73**, 195408 (2006).
- [34] L. Brey and H. A. Fertig, Electronic states of graphene nanoribbons studied with the Dirac equation, *Phys. Rev. B* **73**, 235411 (2006).
- [35] M. S. Hossain, F. Al-Dirini, F. M. Hossain, and E. Skafidas, High performance graphene nano-ribbon thermoelectric devices by incorporation and dimensional tuning of nanopores, *Sci. Rep.* **5**, 11297 (2015).
- [36] S. E. Shafranjuk, Electromagnetic properties of graphene junctions, *Eur. Phys. J. B* **80**, 379 (2011).
- [37] E. Yablonovich, Inhibited Spontaneous Emission in Solid-State Physics and Electronics, *Phys. Rev. Lett.* **58**, 2059 (1987).
- [38] T. Pickering, J. M. Hamm, A. F. Page, S. Wuestner, and O. Hess, Cavity-free plasmonic nanolasing enabled by dispersionless stopped light, *Nat. Commun.* **5**, 4972 (2014).
- [39] J. P. Dowling, M. Scalora, M. J. Bloemer, and C. M. Bowden, The photonic band edge laser: A new approach to gain enhancement, *J. Appl. Phys.* **75**, 1896 (1994).
- [40] M. Engel, M. Steiner, A. Lombardo, A. C. Ferrari, H. V. L. öhneysen, P. Avouris, and R. Krupke, Light-matter interaction in a microcavity-controlled graphene transistor, *Nat. Commun.* **3**, 906 (2012).
- [41] J. Li, M. Jiang, C. Xu, Y. Wang, Y. Lin, J. Lu, and Z. Shi, Plasmon coupled Fabry-Perot lasing enhancement in graphene/ZnO hybrid microcavity, *Sci. Rep.* **5**, 9263 (2015).
- [42] S. Shafranjuk, *Graphene: Fundamentals, Devices, and Applications* (Pan Stanford, Singapore, 2015).
- [43] S. Shafraniuk, Another approach to the problem of room temperature superconductivity, *Quantum Studies: Math. Found.* **5**, 123 (2018).

- [44] D. Sun, C. Divin, J. Rioux, J. E. Sipe, C. Berger, W. A. de Heer, P. N. First, and Th. B. Norris, Coherent control of ballistic photocurrents in multilayer epitaxial graphene using quantum interference, *Nano Lett.* **10**, 1293 (2010).
- [45] M. Liu, X. Yin, E. Ulin-Avila, B. Geng, Th. Zentgraf, L. Ju, F. Wang, and X. Zhang, A graphene-based broadband optical modulator, *Nature (London)* **474**, 64 (2011).
- [46] T. Mueller, F. N. Xia, and P. Avouris, Graphene photodetectors for high-speed optical communications, *Nat. Photonics* **4**, 297 (2010).
- [47] Q. Bao, H. Zhang, B. Wang, Zh. Ni, C. Haley, Y. X. Lim, Y. Wang, D. Y. Tang, and K. P. Loh, Broadband graphene polarizer, *Nat. Photonics* **5**, 411 (2011).
- [48] A. H. Castro Neto, F. Guinea, N. M. R. Peres, K. S. Novoselov, and A. K. Geim, The electronic properties of graphene, *Rev. Mod. Phys.* **81**, 109 (2009).
- [49] M. L. Nesterov, J. Bravo-Abad, A. Yu. Nikitin, F. J. Garcia-Vidal, and L. Martin-Moreno, Graphene supports the propagation of subwavelength optical solitons, *Laser Photonics Rev.* **7**, L7 (2013).
- [50] D. Rodrigo, T. Low, D. B. Farmer, H. Altug, and P. Avouris, Plasmon coupling in extended structures: Graphene superlattice nanoribbon arrays, *Phys. Rev. B* **93**, 125407 (2016).
- [51] M. Mattheakis, C. A. Valagiannopoulos, and E. Kaxiras, Epsilon-near-zero behavior from plasmonic Dirac point: Theory and realization using two-dimensional materials, *Phys. Rev. B* **94**, 201404(R) (2016).
- [52] I. S. Nefedov, C. A. Valagiannopoulos, and L. A. Melnikov, Perfect absorption in graphene multilayers, *J. Opt.* **15**, 114003 (2013).